mater.scichina.com link.springer.com

Published online 12 March 2024 | https://doi.org/10.1007/s40843-023-2818-6
Sci China Mater 2024, 67(4): 1209–1216

SPECIAL TOPIC: Computation-assisted Materials Screening and Design

Two-dimensional alkali auride bimetallene semiconductors

Kai Zhang[1,2], Haifeng Lv[2], Xiaojun Wu[1,2*] and Jinlong Yang[1,2]

ABSTRACT Alloying different metal elements to form two-dimensional (2D) materials (metallenes) holds great significance for both fundamental research and practical applications in nanoelectronics, but few of them are semiconductors with intrinsic band gaps. Here, inspired by bond characteristics in ionic crystals, we report a family of lattice dynamically stable 2D alkali auride bimetallene semiconductors with ionic bonding between alkali and gold atoms by extensive structure search and bonding analysis *via* high-throughput first-principles calculations over 2500 bimetallenes. Among them, 32 2D alkali auride bimetallenes are semiconductors with large band gaps ranging from 0.97 to 5.20 eV due to the large difference in electronegativity between alkali and gold atoms. Exceptionally, 2D LiAu bimetallene is metallic due to the reduced electronegativity difference between Li and Au atoms. Born-Oppenheimer molecular dynamic simulations imply that 19 alkali auride bimetallenes are structurally stable at room temperature for practical applications. This study provides guidance for designing bimetallene semiconductors and deepens the understanding of the correlation between the bonding behavior and electronic properties of 2D metal alloys.

Keywords: bimetallene, ionic bond, semiconductor, first-principles

INTRODUCTION

Metallenes, a graphene analog composed purely of low-coordinated metal atoms, have attracted considerable attention for their fascinating properties, ranging from high catalytic activity, large conductivity, and strong surface plasmon resonance to room-temperature ferromagnetism, as well as promising applications in electronics, topological insulators, superconductors, spintronics, and energy conversion and storage [1–12]. As two-dimensional (2D) morphology is not thermodynamically favorable compared with its close-packed bulk structure, 2D anisotropic growth of metallenes can be achieved experimentally by bottom-up or top-down methods in past years [1,4], such as space- or ligand-confined method [13,14], template-directed growth [15], liquid-phase preparation [16], and solid-melt exfoliation [17]. To date, a variety of compositions and atomic arrangements have been realized, but most reported metallenes exhibit metallic behavior with the exception of some 2D *p*-block metals and alloys [18–22]. The metallic bond dominated interatomic interactions in the metallene lattice due to the pure metal element composition leading to the overlap of the outer electron shells between neighboring atoms, facilitating the free movement of the valence electrons, which is reflected by the energy band crossing the Fermi level in the band structure. However, the lack of a band gap significantly hinders its application in optoelectronics, photocatalysis, and semiconductor-based devices. Therefore, exploring an effective strategy to obtain semiconducting metallenes is highly desirable.

Solid ionic crystals, which are characterized by ionic bonding between cations and anions with large electronegativity differences, usually present wide electronic band gaps [23–25]. Inspired by the bonding characteristics in solid ionic crystal semiconductors, alloying two metal elements with large electronegativity difference could be an instructive method to obtain 2D semiconducting bimetallene. In past years, alloying noble and alkali metals has generated various bulk alloys with exotic properties [23,26–35]. Among them, some synthesized bulk ionic alloys, such as CsAu [23,24,26], RbAu [23], Cs_2Pt [36], and the predicted one-dimensional (1D) CsAu binary linear chain [37], exhibit nonzero electronic band gaps. Meanwhile, some metal alloys, such as K_2Ni compounds [38], could be transformed into a semiconductor under high pressures because the electron configuration and electronegativity of the atoms would be dramatically changed after compression [39–41].

Herein, we report a family of 2D alkali auride bimetallenes with ionic bonding between alkali and gold atoms *via* high-throughput first-principles calculations and a global structure search. A total of 32 bimetallene semiconductors with lattice dynamic stability were obtained from over 2500 bimetallenes with a 1:1 atomic ratio by the proposed high-throughput workflow screening. The estimated band gaps of these bimetallene semiconductors range from 0.97 to 5.20 eV, and some of them can be classified as ultrawide band gap (UWBG) semiconductors [42,43]. After replacing the Cs atom with other alkali metals within the same lattice, the ionicity of M–Au bonds increases monotonically, and the band gaps of alkali auride bimetallenes can emerge as the alkali metal changes from Li to Cs, indicating the significance of the electronegativity difference in the formation of bimetallene semiconductors. We also find that the Cs_2Au_2 bimetallene semiconductor, which has ionic

[1] School of Chemistry and Materials Sciences, CAS Key Lab of Materials for Energy Conversion, Key Laboratory of Precision and Intelligent Chemistry, Collaborative Innovation Center of Chemistry for Energy Material (iChEM), and CAS Center for Excellence in Nanoscience, University of Science and Technology of China, Hefei 230026, China
[2] Hefei National Research Center of Physical Sciences at the Microscale, University of Science and Technology of China, Hefei 230026, China
* Corresponding author (email: xjwu@ustc.edu.cn)

bonding similar to the bulk CsAu alloy, is possibly obtained by exfoliation of the existing $CsAu{\cdot}NH_3$ crystal and could serve as an ideal candidate for experimental exploration [23,44,45]. Our study opens an avenue for the exploration of metallene semiconductors on the basis of the electronegativity of the metal element.

EXPERIMENTAL SECTION

All first-principles calculations were performed based on density functional theory as implemented in the Vienna *ab initio* simulation package (VASP) code [46,47]. The projector augmented wave (PAW) method was used to treat the core electrons and to incorporate the associated relativistic effects of gold [47,48]. The exchange-correlation functional was treated by the generalized gradient approximation (GGA) with Perdew-Burke-Ernzerhof (PBE) parameterization for plane-wave expansions with a cutoff energy of 500 eV [49]. A vacuum space larger than 15 Å was used to eliminate the interactions between adjacent periodic images of metallenes. All metallenes were optimized until the energy and forces converged to 10^{-6} eV and 10^{-3} eV Å^{-1}, respectively. The Γ-centered *k*-meshes with a space resolution of at least $2\pi \times 0.02$ Å^{-1} for Brillouin zone sampling were used to ensure well-converged energy calculations. The PBE functional was used to evaluate whether a bimetallene is a metal or a semiconductor, and the hybrid PBE0 functional was used to calculate the band gaps of bimetallene semiconductors [50]. The lattice dynamical stability was confirmed by phonon spectrum calculations using the finite displacement approach as implemented in the PHONOPY code [51]. Born-Oppenheimer molecular dynamics (BOMD) simulations were performed within an NVT canonical ensemble using the Nosé-Hoover thermostat at different temperatures for 5 ps with a time step of 1 fs [52,53].

The structure search was carried out by using an unbiased swarm intelligence method as implemented in the CALYPSO program to explore bimetallenes [54,55]. The ability to predict the ground state or metastable structures based only on the known chemical composition is the key feature of this method [56]. For alkali metal auride systems with a 1:1 atomic ratio and monometallenes, the candidate structures were predicted using a simulation cell containing two, four, and eight atoms. For KAu bimetallenes with various atomic ratios (1:7–7:1), a simulation cell with eight atoms was used. The structure search would be terminated if positive enthalpies were formed in the generated metallenes.

Natural resonance theory (NRT) analysis was conducted using the Natural Bond Orbital (NBO 7.0) and Gaussian16 program packages to evaluate the ionicity of alkali metal-gold bonds with different coordination environments [57–60]. The charge transfers were calculated by Bader charge analysis [61]. The chemical bonding analysis of bimetallenes was completed by calculating the Crystal Orbital Hamilton Population (COHP) and their integrals (ICOHP), which were carried out by employing the LOBSTER 4.1.0 code [62–66].

RESULTS AND DISCUSSION

The inherent semiconductor characteristics of bulk alkali auride alloys with unique metal-metal ionic bonds suggest that 2D bimetallene semiconductors are expected to be obtained by alloying gold and alkali metals in 2D space. However, if the atomic ratio of M:Au deviates far from 1:1, M–M or Au–Au metallic bonds tend to form in M_nAu_m bimetallenes, thus hindering the formation of the band gap. Here, we take K_nAu_m bimetallene as a prototype by performing an extensive structure search on 2D K_nAu_m (n = 0 to 7, and m = 8 – n). The global minimum structure for each composition and the relative energy evolution of different structures of K_nAu_m are shown in Fig. 1 and Fig. S1. When the K:Au ratio is close to 1:1, the K atoms, Au atoms, and K–Au bonds show a distinct homogeneous distribution, which suggests that the ratio of the K–Au bonds is high. The electronic band structures of the lowest energy 2D K metallene, Au metallene and K_mAu_n bimetallene are shown in Fig. 1a–i. 2D K_5Au_3, K_4Au_4, K_3Au_5 and K_2Au_6 bimetallenes are semiconductors. Fig. 1j summarizes the evolution of K–Au bond percentages and band gaps of K_nAu_m bimetallenes with composition. The percentage of K–Au bond increases from 0% in K metallene to 66.7% in K_4Au_4 bimetallene, and then gradually decreases to 0% in Au metallene. The percentage of K–Au bond is the highest when the K:Au ratio reaches 1:1, which leads to the largest band gap in K_4Au_4 bimetallene. This confirms our hypothesis that M:Au = 1:1 favors the formation of bimetallene semiconductors. In the following, we will focus on the global structure of MAu (M = Li, Na, K, Rb and Cs) bimetallenes with an atomic ratio of 1:1.

Next, a high-throughput DFT screening workflow was carried out to obtain various alkali auride bimetallene semiconductors, as shown in Fig. 2. First, the initial bimetallene structures were generated from the given chemical compositions using the particle swarm prediction method. Fig. S2 shows the evolution of the relative energies and the formation energies of more than 2500 generated alkali auride bimetallenes. Second, we performed structural optimization on the generated alkali auride bimetallenes and calculated the formation energies E_f, which are defined as $E_f(MAu) = [E(M_xAu_x) - xE(Cs) - xE(Au)]/2x$, where $E(M_xAu_x)$ is the total energy of M_xAu_x per unit cell, and $E(M)$ and $E(Au)$ are the total energies per atom of elemental alkali metal and gold solids, respectively. The calculated negative value of formation energies indicates that the formation of 1258 alkali auride bimetallenes from the corresponding alkali and gold bulks is thermodynamically feasible. We then screened bimetallene semiconductors by eliminating duplicate structures and calculating the band gap at the level of the PBE functional. Note that the PBE functional always underestimates the band gap values of semiconductors, but it still allows for quick identification of bimetallene semiconductors.

The phonon spectra of the screened semiconductors were then calculated, and only 32 bimetallene semiconductors are lattice dynamically stable, including 3 structures of NaAu, 7 structures of KAu, 11 structures of RbAu, and 11 structures of CsAu bimetallenes, as shown in Fig. S3. In addition, several metallic bimetallenes of LiAu are also lattice-dynamically stable (see Fig. S4 and Table S1). Table S2 summarizes the lattice parameters, atomic coordinates and symmetry information of the 32 bimetallene semiconductors.

The average formation energies per atom of 32 bimetallenes are summarized in Table S3. The calculated formation energies of these semiconductors are lower than −60 meV atom^{-1}, but are larger than that of the bulk CsAu alloy (−325 meV atom^{-1}) due to their high specific surface area (Fig. S5). BOMD simulations were further performed to check the lattice thermodynamical stability. Here, bimetallenes with the same chemical composition (MAu-*n*) are numbered according to their forma-

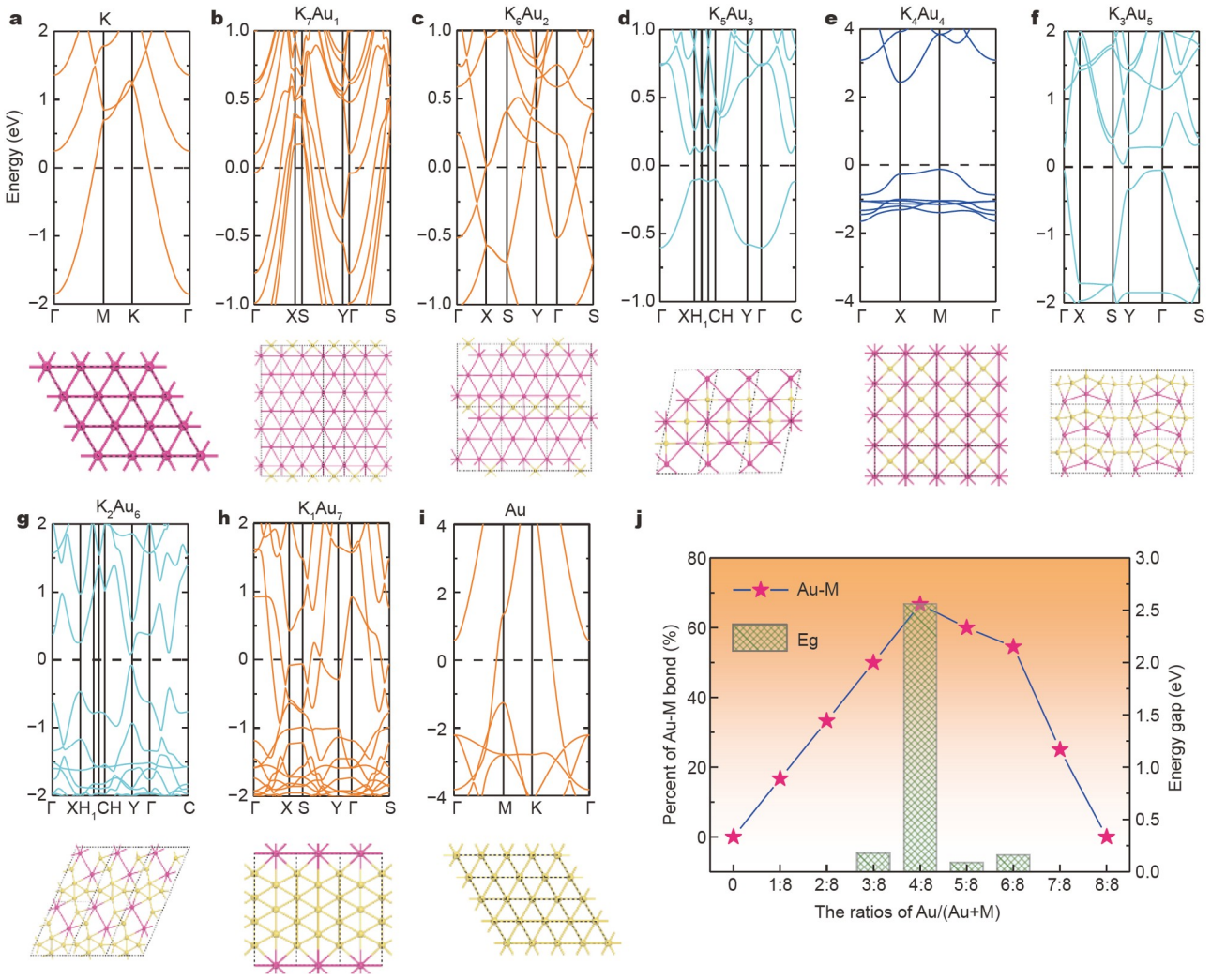

Figure 1 The band structures and atomic arrangement of monolayer (a) K metallene, (b) K_7Au_1, (c) K_6Au_2, (d) K_5Au_3, (e) K_4Au_4, (f) K_3Au_5, (g) K_2Au_6, (h) K_1Au_7 bimetallene, and (i) Au metallene. (j) Evolution of the Au–M bond percentage and band gap of metallenes with composition. The K and Au atoms are indicated by red and yellow balls, respectively.

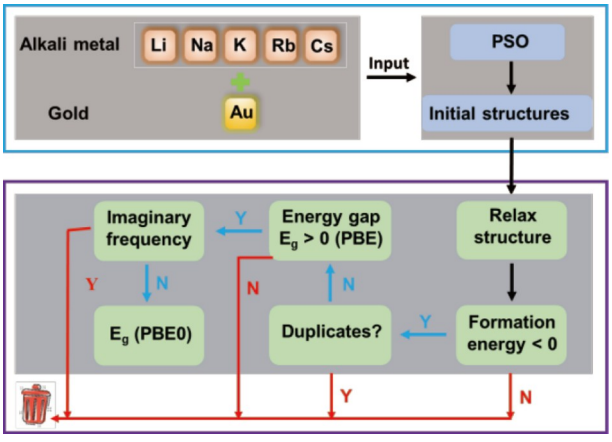

Figure 2 The workflow of high-throughput screening MAu bimetallene semiconductors.

tion energies, where n = 1 represents the one that has the lowest formation energy. NaAu-3, KAu-3, and CsAu-7 cannot maintain their lattice structures even at 100 K, indicating that they are not suitable for practical application at room temperature, as shown in Fig. S6. In addition, the lattices of NaAu-1, RbAu-7, RbAu-8, CsAu-4, CsAu-5, CsAu-6, and CsAu-8 collapse, while KAu-4, KAu-6, and RbAu-3 retain their 2D lattices at 200 K after 5 ps simulations. The remaining 19 bimetallenes can maintain their lattice structures at room temperature after 5 ps simulations, indicating that these bimetallene semiconductors are promising for a wide range of applications.

The predicted bimetallene semiconductors exhibit quite crystal structure differences, including symmetry, coordination number, unit cell, and bond lengths, despite having the same stoichiometry. Seven representative structures belonging to different space groups are displayed in Fig. 3a. NaAu-1 adopts a well-known α-FeSe type structure (space group *Pmmn*) and contains two formula units per cell. Each Na (Au) atom is surrounded by four neighboring Au (Na) atoms and thus forms an edge-shared Na–Au tetrahedron network. The nearest Na–Au, Na–Na, and Au–Au distances are 2.96, 3.78, and 4.55 Å. NaAu-2 belongs to $P\bar{1}$ space group with four formula units per cell. Each Au atom is bound to six Na atoms and located at the center of Au_6 triangular prism with the shortest Na–Au bond

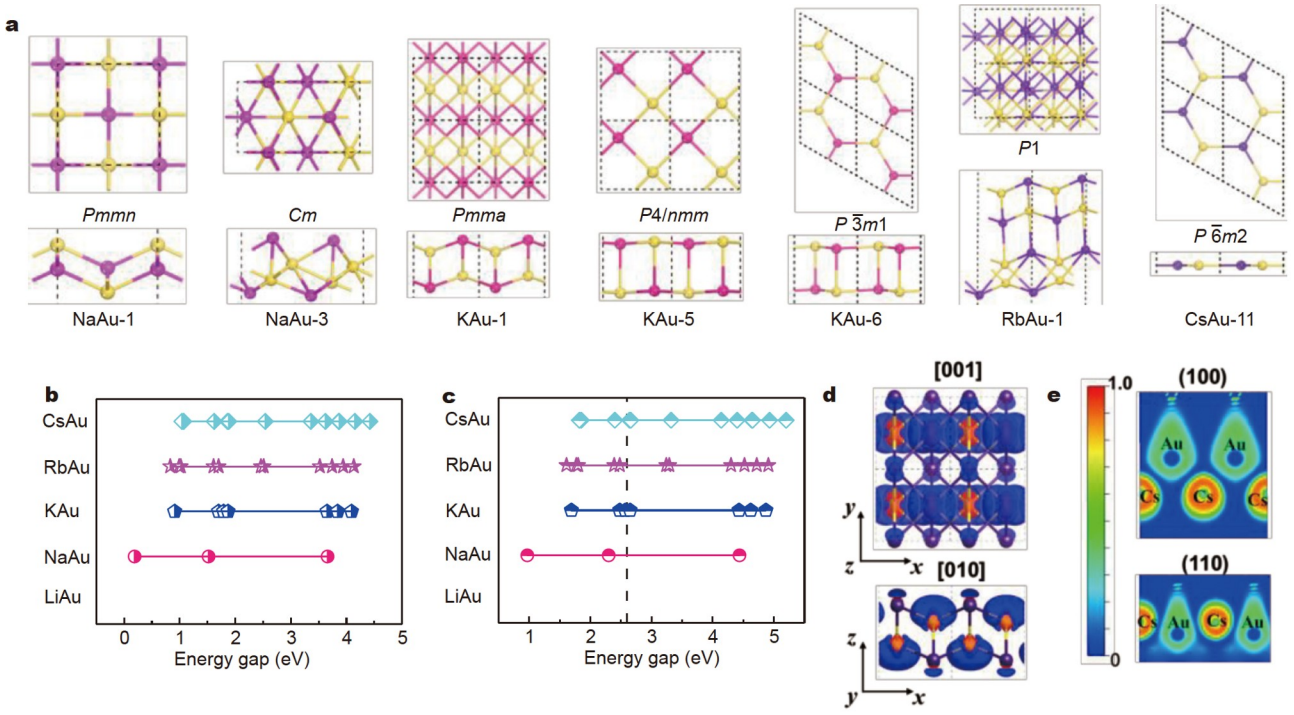

Figure 3 (a) Seven representative structure types out of 32 bimetallene semiconductors. (b) The calculated band gaps of the screened MAu bimetallene semiconductors by using the PBE0 functional. (c) The revised band gaps take into account the underestimation of the PBE0 functional, and the experimentally measured band gap of bulk CsAu is indicated by the black dashed lines. (d) The charge density difference of CsAu-1 with isovalue of 2×10^{-3} e$^-$ Bohr^{-3}. (e) ELF of CsAu-1.

length of 2.98 Å (Fig. S7 and Table S3). NaAu-3 has four Au and four Na atoms in a unit cell with *Cm* symmetry. There, Au atoms form a puckered graphene-like arrangement, while half of the Na atoms are located on top of the Au atoms and the other Na atoms are situated below the Au hexagon. The nearest Na–Au and Au–Au distances are 2.81 and 2.88 Å, respectively. KAu-1 stabilizes into *Pmma* symmetry with two formula units per cell. The Au atoms are shifted towards each other, forming zigzag chains with short K–Au and Au–Au separation of 3.38 and 2.95 Å, respectively. Each Au atom is surrounded by six Cs atoms and has a triangular prism coordination geometry. For KAu-5, the structure consists of two K–Au square sublayers and belongs to the *P*4/*nmm* space group. Each Na (Au) atom directly bonds to five Au (Na) atoms with four equal K–Au bond lengths of 3.36 Å and one K–Au distance of 3.39 Å. KAu-6 (space group $P\bar{3}m1$; two formula units per cell) contains two *h*-BN-like sublayers with honeycomb sublayers bonded to each other by K–Au bond along out-of-plane direction. Both K and Au atoms have a coordination number of four, and three equal K–Au bond length is 3.29 Å while the other K–Au separation is 3.36 Å. The lowest formation energy in RbAu-1 among the searched RbAu bimetallene semiconductors can be ascribed to its 3D-like networks. Its unit cell contains four formula units and eight atomic layers with *P*1 symmetry. It could be viewed as one KAu-1-like sublattice rotated 90° and then bonding with the other KAu-1-like sublattice. We also find that CsAu-11 is the only bimetallene semiconductor possessing a monoatomic planar structure with a Cs-Au distance equal to 3.47 Å. It has similar lattice symmetry and atomic arrangement (space group $P\bar{6}m2$; one formula unit per cell) with monolayer *h*-BN. In addition, as shown in Fig. S7, RbAu-2 and CsAu-1 have the same symmetry with KAu-1, while KAu-7, RbAu-11, and CsAu-10 share the same space group of *Pmmn* with NaAu-1. The optimized lattice parameters of CsAu-1 are a = 5.04 Å and b = 4.87 Å. The calculated Au–Au distance (d_{Au-Au}) along the zigzag chain of Au atoms and the average Cs–Au distance (d_{Cs-Au}) are 3.00 and 3.66 Å, respectively, which are in agreement with the experimental values of d_{Au-Au} = 3.02 Å and d_{Cs-Au} = 3.65 Å in the CsAu·NH$_3$ crystal [44]. RbAu-4 and CsAu-3 have KAu-5-like lattices while RbAu-10 has a similar honeycomb lattice to KAu-6. Other bimetallene semiconductors with low-symmetry (space group *P*1 or $P\bar{1}$), such as NaAu-2, KAu-2, RbAu-3, RbAu-5, CsAu-2, and CsAu-7, also exhibit diverse atomic arrangements and coordination environments (Fig. S7 and Table S3).

The electronic structures of 32 bimetallene semiconductors were calculated using a hybrid PBE0 functional. Test calculation indicates that the PBE0 functional has better performance than the PBE and HSE06 functionals in estimating the band gap of the synthesized bulk CsAu, as shown in Fig. S8. The calculated electronic band structures of 32 bimetallene semiconductors are shown in Fig. S9. The band gaps of NaAu, KAu, RbAu and CsAu bimetallene semiconductors range from 0.19 to 3.66 eV, from 0.91 to 4.09 eV, from 0.83 to 4.13 eV and from 1.04 to 4.42 eV (Fig. 3b), respectively. Note that the calculated band gap of bulk CsAu with PBE0 functional is about 0.78 eV smaller than the experimental value (2.6 eV) (Fig. S8) [24]. A scissor parameter of 0.78 eV is used to adjust the calculated band gap of 32 bimetallene semiconductors, as shown in Fig. 3c. It is worth noting that 1 structure of NaAu (NaAu-1), 3 structures of KAu (KAu-6, KAu-7, KAu-5), 4 structures of RbAu (RbAu-10, RbAu-11, RbAu-4, RbAu-6), and 5 structures of CsAu (CsAu-11, CsAu-9, CsAu-10, CsAu-3, CsAu-4) bimetallenes are ultrawide band gap

(UWBG) semiconductors, and their band gaps are larger than traditional wide bandgap semiconductors SiC (3.2 eV) and GaN (3.4 eV) [42,43]. In particular, considering the scissor parameter, the band gap of CsAu-11 bimetallene reaches 5.2 eV, which is comparable to the experimentally realized UWBG semiconductors Ga_2O_3 (4.9 eV) and diamond (5.5 eV) [43].

Next, the nature of chemical bonding between alkali metal and gold in MAu bimetallene semiconductors was explored. The evolution of M–Au bond character and electronic structures with electronegativity differences in the MAu alloy were also investigated. As displayed in Fig. S10a, the chemical formula M_2Au_2 with *Pmma* space group was adopted as a prototype, which is repeatedly found in predicted MAu bimetallenes (such as KAu-1, RbAu-2 and CsAu-1), and the lattice symmetry of the synthesized CsAu was used to model the bulk MAu alloy (Fig. S10b). The structural information of the five MAu bimetallenes and five bulk MAu alloys is summarized in Table S4. The bonding strength between the alkali metal and gold atoms can be revealed by the value of ICOHP. As illustrated in Fig 4a, the absolute ICOHP values of M–Au pairs in M_2Au_2 bimetallenes and bulk MAu alloys both decrease when the alkali metal changes from Cs to Na, and then increase for the LiAu alloy. Overall, the absolute ICOHP values of M–Au pairs in M_2Au_2 bimetallenes are lower than those in MAu bulk alloys, suggesting a relatively weaker but still comparable bonding strength with bulk alloys. The evolution of the M–Au bonding strength is also evidenced by the formation energy. Fig. 4b shows that the formation energies of both AuM bimetallenes and bulk alloys show a similar trend when the Cs atom is replaced by other alkali metals, which is consistent with the variation tendency of the ICOHP values since stronger bonding usually results in a more thermodynamically stable structure. The strong interaction between alkali metal and gold atoms was also manifested by Bader charge analysis. The results show that the electrons transferred from alkali metal to gold atoms range from 0.74 to 0.82 e^- Au^{-1} and from 0.76 to 0.85 e^- Au^{-1} for bimetallenes and bulk alloys (Figs 3d, 4c and Fig. S10c), respectively. As shown in Fig. 3e, Figs S10d and S11, the plotted electron localization function (ELF) shows that delocalized and localized electrons are clearly distributed around Au and alkali metal atoms, respectively, with very low ELF values in the interstitial region along the M–Au direction in both CsAu, RbAu and KAu bimetallenes and bulk alloys, indicating a typical ionic bonding character. Although the electrons around Na or Li atoms are more delocalized than those on Cs, Rb or K atoms, there are still no obvious shared electrons localized in the interstitial region, suggesting that the bonds between Au and Na or Li atoms could also be recognized as ionic bonds. The ionic nature of the M–Au bond is further confirmed by performing NBO analysis. As shown in Fig. 4d and Fig. S12, the average ionicity of the M–Au bond ranges from 76.2% to 97.9% and from 75.4% to 99.9% for AuM_6 and AuM_8 clusters, respectively, with the values in AuM_6 and the corresponding AuM_8 clusters being close to each other. The average ionicity of M–Au bond decreases monotonically as M changes from Cs to Rb, K, Na and Li, which agrees well with the observation of ELF maps, as expected from the consideration of electronegativity differences between alkali metal and gold. The detailed comparison between CsAu-1 and bulk CsAu is shown in Fig. S10. In general, the large charge transfer, localized electron distribution, strong M–Au bonding in MAu bimetallenes together with pronounced ionicity of M–Au bonds in MCs_6 cluster present compelling evidence that the ionic M–Au bond, which had been observed in bulk MAu alloys, can also be stabilized in two dimensions.

The intrinsic band gap in the searched bimetallene semiconductors could be ascribed to the enhanced ionic bonding and limited metallic bonding character. As shown in Figs S8 and S13, bulk CsAu and RbAu are semiconductors with band gaps of 1.06 and 0.42 eV, respectively, while bulk KAu, NaAu, and LiAu transition to metals at PBE functional level, which is consistent

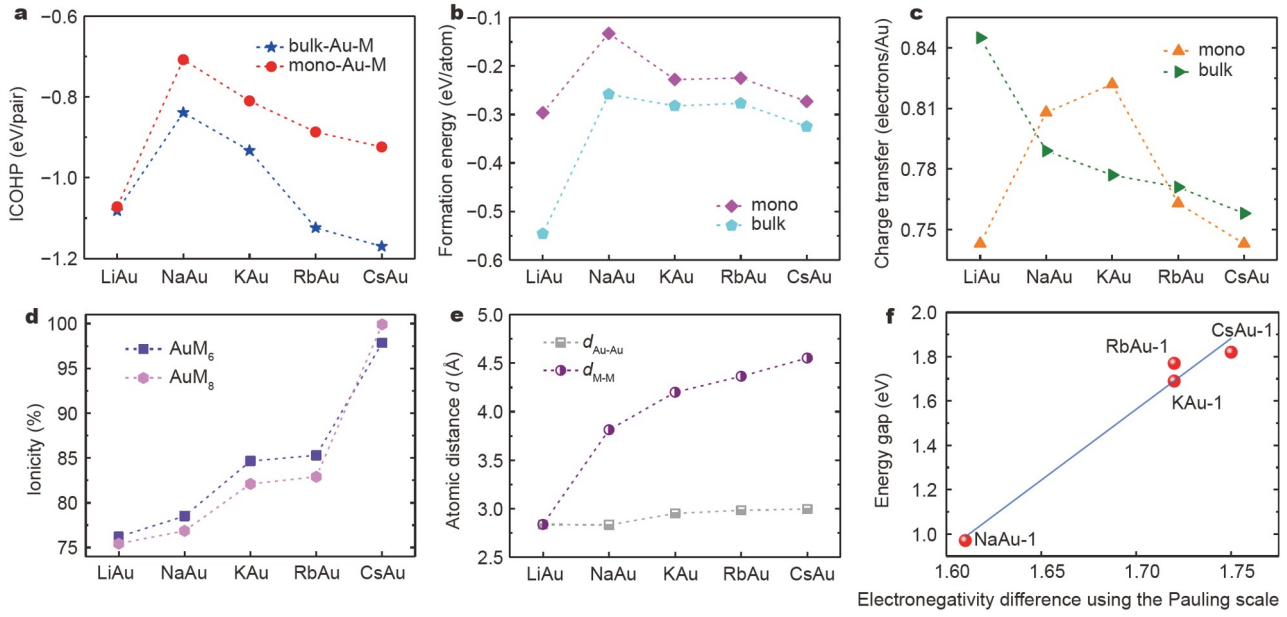

Figure 4 The evolution of (a) integrated crystal orbital Hamilton populations (ICOHP), (b) formation energies, (c) charge transfer, and (d) ionicity of the Au–M bond of 2D and bulk MAu alloys. (e) The smallest Au–Au and M–M distances of MAu bimetallenes and bulk alloys. (f) The linear relationship between the band gap and the electronegativity difference of four bimetallene semiconductors with the lowest formation energy, the electronegativity of K and Rb, is identical when using the Pauling scale.

with previous studies [23,67,68]. Similarly, CsAu and RbAu bimetallene are also semiconductors with small band gaps of 0.27 and 0.18 eV, respectively, while NaAu and LiAu bimetallenes with *Pmma* symmetry are metals, as displayed in Figs S10 and S13. However, the KAu bimetallene becomes a semiconductor with a band gap of 0.16 eV. The occurrence of band gaps in MAu alloys can also be controlled by the M–M and Au–Au distances. As revealed in Fig. 4e, the smallest distances of M–M and Au–Au increase monotonically from Li to Cs, indicating a weaker metallic bonding of M–M and Au–Au and thus less metallicity in electronic structures. At the same time, the Au alone becomes more free-atom-like and tends to open an energy gap at FL with increasing size of the alkali metal atoms, but Li and Na act to close the gap completely [69]. Therefore, the iconicity of the M–Au bond and the band gap of MAu alloy are positively related to the electronegativity difference between alkali metal and gold within the same lattice symmetry. The above discussions also qualitatively explain why no LiAu bimetallene semiconductor has been achieved by screening.

The charge transfers of 32 bimetallene semiconductors are displayed in Table S3. As found in CsAu-1, electrons are also transferred from alkali metal to gold in other 31 MAu bimetallenes, and the charge transfer values in most bimetallenes are larger than that of bulk CsAu (Fig. S14). Furthermore, the ELF profiles of 32 semiconductors were plotted in Fig. S15. Similarly, the low ELF value and the absence of shared electrons in the interstitial region along the M–Au bond, also indicate the ionic bonding characteristic in 31 other bimetallene semiconductors. We also notice that the bimetallene semiconductors with the smallest band gap within the same chemical composition are first- or second-energy-favorable structures. Especially, the band gaps of the four most energy favorable bimetallene semiconductors (NaAu-1, KAu-1, RbAu-1, and CsAu-1) almost present a linear relationship with electronegativity difference, as shown in Fig. 4f. The family of alkali auride bimetallene semiconductors confirm that the electronegativity difference can be a guideline for the design of bimetallene semiconductors.

For practical applications, these bimetallene semiconductors should be stabilized in ambient conditions. The interaction between 19 bimetallenes, which could maintain their lattices after 5 ps molecular dynamics simulations at room temperature, and oxygen molecules were then calculated. The results suggest that NaAu-2, KAu-1, KAu-2, RbAu-1, RbAu-2, RbAu-7, CsAu-1, and CsAu-2 would be unstable when exposed to air, as indicated by the large oxygen molecule adsorption energy (Table S5 and Fig. S16). The large distance between the remaining eleven bimetallenes and oxygen ranges from 3.01 to 3.61 Å, suggesting their resistance to oxidation.

Then, the carrier mobility was estimated based on the deformation theory. Table S6 shows the intrinsic electron and hole mobilities of these bimetallene semiconductors range from 0.2 to 75,579.6 $cm^2 V^{-1} s^{-1}$ and from 5.0 to 186,722.1 $cm^2 V^{-1} s^{-1}$ at room temperature, respectively. Especially, the carrier mobility of NaAu-2, KAu-2, RbAu-4, RbAu-6, CsAu-3 and CsAu-10 is comparable to that of graphene and graphyne. Further, the light absorption spectra of nineteen bimetallenes were calculated. Fig. S17 shows that both infra-red, visible and ultra-violet dominated light absorption can be found in these bimetallenes. Moreover, the parallel AA-stacking mode was adopted to estimate the interlayer interaction of nineteen alkali auride bimetallenes. The binding energy E_b of bilayer bimetallene was calculated using $E_b = E_{bi} - E_{mono}$, where E_{bi} and E_{mono} are the energy of AA-stacked bilayer and pristine monolayer bimetallene. Table S7 shows that the E_b of these bilayer bimetallenes is comparable to that of bilayer MoS_2, indicating the interlayer interaction is of the van der Waals type, except for NaAu-2, which has a large interlayer binding energy.

We notice that the screened CsAu-1 with *Pmma* symmetry is an integral part of the lattice of the experimentally realized quasi-lamellar $CsAu{\cdot}NH_3$ crystal [44], as shown in Figs S10a and S18. In addition, the calculated formation energy of CsAu-1 is -0.273 eV $atom^{-1}$, comparable to that of bulk CsAu (-0.325 eV $atom^{-1}$), indicating that the synthesis of CsAu-1 from elemental Cs and Au solids is exothermic and thermodynamically feasible. The lattice stability of CsAu-1 was also confirmed by phonon dispersion spectrum and BOMD simulations as mentioned above (Figs S3 and S6). Further, we find the lattice of Cs_2Au_2 bimetallene can be maintained at the temperatures up to 500 K (Fig. S19). Although the d-block bimetallene semiconductor has not been synthesized in experiments, CsAu-1, which is possibly synthesized *via* exfoliation of $CsAu{\cdot}NH_3$ along the (001) plane or controllable growth on a suitable substrate, could be an ideal candidate for experimental verification. Similarly, other $MAu{\cdot}NH_3$ are possibly formed by dissolving bulk MAu alloys in liquid ammonia [44], and then MAu bimetallene can be obtained by exfoliation. Moreover, we also find some metallic NaAu, RbAu, and CsAu bimetallenes are dynamically stable (Fig. S20).

CONCLUSIONS

In summary, the realization of bimetallene semiconductors by alloying different metal elements with large electronegativity differences is proposed. We have performed high-throughput calculations and structural searches to screen alkali auride bimetallene semiconductors with an atomic ratio of 1:1, which exhibit a superior ability to introduce a band gap than other ratios. As a result, 32 bimetallene semiconductors, including 3 NaAu, 7 KAu, 11 RbAu, and 11 CsAu bimetallenes with lattice dynamic stability, were obtained from over 2500 bimetallenes after screening. Among them, 19 bimetallenes could maintain their 2D lattices at room temperature. The estimated band gaps of NaAu, KAu, RbAu, and CsAu bimetallene semiconductors are range from 0.97 to 4.44 eV, from 1.69 to 4.87 eV, from 1.61 to 4.91 eV, and from 1.82 to 5.20 eV, respectively. It is noteworthy that the band gaps of some bimetallenes reach the range of UWBG semiconductors, which has never been observed in metal alloys before. Furthermore, by replacing Cs with other alkali metals within the same lattice, we find that the iconicity of the M–Au bond and the band gap of MAu alloy are positively related to the electronegativity difference. We also notice that the CsAu-1 bimetallene is possibly obtained by exfoliation of the experimentally realized $CsAu{\cdot}NH_3$ crystal. Our results unveil that the electronegativity difference could be an effective indicator for searching bimetallene semiconductors.

Received 27 November 2023; accepted 8 February 2024; published online 12 March 2024

1 Wu J, Zhao X, Cui X, *et al.* Emerging two-dimensional metallenes: Recent advances in structural regulations and electrocatalytic applications. Chin J Catal, 2022, 43: 2802–2814
2 Liu Y, Dinh KN, Dai Z, *et al.* Metallenes: Recent advances and opportunities in energy storage and conversion applications. ACS Mater

Lett, 2020, 2: 1148–1172
3 Cao C, Xu Q, Zhu QL. Ultrathin two-dimensional metallenes for heterogeneous catalysis. Chem Catal, 2022, 2: 693–723
4 Xie M, Tang S, Zhang B, *et al.* Metallene-related materials for electrocatalysis and energy conversion. Mater Horiz, 2023, 10: 407–431
5 Ta HQ, Mendes RG, Liu Y, *et al. In situ* fabrication of freestanding single-atom-thick 2D metal/metallene and 2D metal/metallene oxide membranes: Recent developments. Adv Sci, 2021, 8: 2100619
6 Prabhu P, Lee JM. Metallenes as functional materials in electrocatalysis. Chem Soc Rev, 2021, 50: 6700–6719
7 Huang X, Tang S, Mu X, *et al.* Freestanding palladium nanosheets with plasmonic and catalytic properties. Nat Nanotech, 2011, 6: 28–32
8 Nevalaita J, Koskinen P. Atlas for the properties of elemental two-dimensional metals. Phys Rev B, 2018, 97: 035411
9 Li W, Qiu X, Lv B, *et al.* Free-standing 2D ironene with magnetic vortex structure at room temperature. Matter, 2022, 5: 291–301
10 Reis F, Li G, Dudy L, *et al.* Bismuthene on a SiC substrate: A candidate for a high-temperature quantum spin Hall material. Science, 2017, 357: 287–290
11 Zhang T, Cheng P, Li WJ, *et al.* Superconductivity in one-atomic-layer metal films grown on Si(111). Nat Phys, 2010, 6: 104–108
12 Luo M, Zhao Z, Zhang Y, *et al.* PdMo bimetallene for oxygen reduction catalysis. Nature, 2019, 574: 81–85
13 Duan H, Yan N, Yu R, *et al.* Ultrathin rhodium nanosheets. Nat Commun, 2014, 5: 3093
14 Funatsu A, Tateishi H, Hatakeyama K, *et al.* Synthesis of monolayer platinum nanosheets. Chem Commun, 2014, 50: 8503–8506
15 Zhao J, Deng Q, Bachmatiuk A, *et al.* Free-standing single-atom-thick iron membranes suspended in graphene pores. Science, 2014, 343: 1228–1232
16 Zhang F, He J, Xiang Y, *et al.* Semimetal-semiconductor transitions for monolayer antimonene nanosheets and their application in perovskite solar cells. Adv Mater, 2018, 30: 1803244
17 Kochat V, Samanta A, Zhang Y, *et al.* Atomically thin gallium layers from solid-melt exfoliation. Sci Adv, 2018, 4: e1701373
18 Chen M, Liu F. Prediction of giant and ideal Rashba-type splitting in ordered alloy monolayers grown on a polar surface. Natl Sci Rev, 2021, 8: nwaa241
19 Gou J, Xia B, Li H, *et al.* Binary two-dimensional honeycomb lattice with strong spin-orbit coupling and electron-hole asymmetry. Phys Rev Lett, 2018, 121: 126801
20 Wang X, He J, Zhou B, *et al.* Bandgap-tunable preparation of smooth and large two-dimensional antimonene. Angew Chem Int Ed, 2018, 57: 8668–8673
21 Zhang S, Xie M, Li F, *et al.* Semiconducting group 15 monolayers: A broad range of band gaps and high carrier mobilities. Angew Chem Int Ed, 2016, 55: 1666–1669
22 Forti S, Link S, Stöhr A, *et al.* Semiconductor to metal transition in two-dimensional gold and its van der Waals heterostack with graphene. Nat Commun, 2020, 11: 2236
23 Spicer WE, Sommer AH, White JG. Studies of the semiconducting properties of the compound CsAu. Phys Rev, 1959, 115: 57–62
24 Spicer WE. Photoemission and band structure of the semiconducting compound CsAu. Phys Rev, 1962, 125: 1297–1299
25 Perera S, Hui H, Zhao C, *et al.* Chalcogenide perovskites—An emerging class of ionic semiconductors. Nano Energy, 2016, 22: 129–135
26 Sommer A. Alloys of gold with alkali metals. Nature, 1943, 152: 215
27 Stanek J, Hafner SS, Hensel F. Phase transition of CsAu at high pressure. Phys Rev B, 1985, 32: 3129–3133
28 King RB. Metal cluster topology 19. Beyond the auride ion: Triangulated gold networks and ethane-like structural units in binary and ternary alkali metal gold intermetallics. Inorg Chim Acta, 1998, 277: 202–210
29 Pyykkö P. Theoretical chemistry of gold. Angew Chem Int Ed, 2004, 43: 4412–4456
30 Jansen M. The chemistry of gold as an anion. Chem Soc Rev, 2008, 37: 1826–1835
31 Charpentier N, Clérouin J. *Ab initio* simulations of the liquid alloy Au-Cs. Phys Rev B, 2008, 78: 100202
32 Miao M, Brgoch J, Krishnapriyan A, *et al.* On the stereochemical inertness of the auride lone pair: *Ab initio* studies of AAu (A = K, Rb, Cs). Inorg Chem, 2013, 52: 8183–8189
33 Yang G, Wang Y, Peng F, *et al.* Gold as a 6p-element in dense lithium aurides. J Am Chem Soc, 2016, 138: 4046–4052
34 Xiao C, Wang LL, Maligal-Ganesh RV, *et al.* Intermetallic $NaAu_2$ as a heterogeneous catalyst for low-temperature CO oxidation. J Am Chem Soc, 2013, 135: 9592–9595
35 Du X, Lou H, Wang J, *et al.* Pressure-induced Na–Au compounds with novel structural units and unique charge transfer. Phys Chem Chem Phys, 2021, 23: 6455–6461
36 Karpov A, Nuss J, Wedig U, *et al.* Cs_2Pt: A platinide(-II) exhibiting complete charge separation. Angew Chem Int Ed, 2003, 42: 4818–4821
37 Choi YC, Lee HM, Kim WY, *et al.* How can we make stable linear monoatomic chains? Gold-cesium binary subnanowires as an example of a charge-transfer-driven approach to alloying. Phys Rev Lett, 2007, 98: 076101
38 Adeleke AA, Stavrou E, Adeniyi AO, *et al.* Two good metals make a semiconductor: A potassium-nickel compound under pressure. Phys Rev B, 2020, 102: 134120
39 Rahm M, Cammi R, Ashcroft NW, *et al.* Squeezing all elements in the periodic table: Electron configuration and electronegativity of the atoms under compression. J Am Chem Soc, 2019, 141: 10253–10271
40 Lin J, Zhang S, Guan W, *et al.* Gold with +4 and +6 oxidation states in AuF_4 and AuF_6. J Am Chem Soc, 2018, 140: 9545–9550
41 Zhai H, Xu R, Dai J, *et al.* Stabilized nitrogen framework anions in the Ga–N system. J Am Chem Soc, 2022, 144: 21640–21647
42 Xie C, Lu X, Tong X, *et al.* Recent progress in solar-blind deep-ultraviolet photodetectors based on inorganic ultrawide bandgap semiconductors. Adv Funct Mater, 2019, 29: 1806006
43 Tsao JY, Chowdhury S, Hollis MA, *et al.* Ultrawide-bandgap semiconductors: research opportunities and challenges. Adv Elect Mater, 2018, 4: 1600501
44 Mudring AV, Jansen M, Daniels J, *et al.* Cesiumauride ammonia (1/1), $CsAu{\cdot}NH_3$: A crystalline analogue to alkali metals dissolved in ammonia? Angew Chem Int Ed, 2002, 41: 120–124
45 Wertheim GK, Bates Jr. CW, Buchanan DNE. Electronic structure of CsAu. Solid State Commun, 1979, 30: 473–475
46 Kresse G, Furthmüller J. Efficient iterative schemes for *ab initio* total-energy calculations using a plane-wave basis set. Phys Rev B, 1996, 54: 11169–11186
47 Kresse G, Joubert D. From ultrasoft pseudopotentials to the projector augmented-wave method. Phys Rev B, 1999, 59: 1758–1775
48 Blöchl PE. Projector augmented-wave method. Phys Rev B, 1994, 50: 17953–17979
49 Perdew JP, Burke K, Ernzerhof M. Generalized gradient approximation made simple. Phys Rev Lett, 1996, 77: 3865–3868
50 Adamo C, Barone V. Toward reliable density functional methods without adjustable parameters: The PBE0 model. J Chem Phys, 1999, 110: 6158–6170
51 Togo A, Tanaka I. First principles phonon calculations in materials science. Scripta Mater, 2015, 108: 1–5
52 Nosé S. A unified formulation of the constant temperature molecular dynamics methods. J Chem Phys, 1984, 81: 511–519
53 Hoover WG. Canonical dynamics: Equilibrium phase-space distributions. Phys Rev A, 1985, 31: 1695–1697
54 Wang Y, Lv J, Zhu L, *et al.* Crystal structure prediction *via* particle-swarm optimization. Phys Rev B, 2010, 82: 094116
55 Wang Y, Lv J, Zhu L, *et al.* CALYPSO: A method for crystal structure prediction. Comput Phys Commun, 2012, 183: 2063–2070
56 Zhang K, Chen M, Wang D, *et al.* Nodal-loop half metallicity in a two-dimensional Fe_4N_2 pentagon crystal with room-temperature ferromagnetism. Nanoscale, 2021, 13: 19493–19499
57 Glendening ED, Weinhold F. Natural resonance theory: I. General formalism. J Comput Chem, 1998, 19: 593–609
58 Frisch MJ, Trucks GW, Schlegel HB, *et al.* Gaussian 16 rev. C.01. Secondary Gaussian 16 rev. C.01, 2016
59 Reed AE, Curtiss LA, Weinhold F. Intermolecular interactions from a natural bond orbital, donor-acceptor viewpoint. Chem Rev, 1988, 88:

899–926
60 Glendening ED, Landis CR, Weinhold F. NBO 7.0: New vistas in localized and delocalized chemical bonding theory. J Comput Chem, 2019, 40: 2234–2241
61 Henkelman G, Arnaldsson A, Jónsson H. A fast and robust algorithm for Bader decomposition of charge density. Comput Mater Sci, 2006, 36: 354–360
62 Maintz S, Deringer VL, Tchougréeff AL, *et al.* LOBSTER: A tool to extract chemical bonding from plane-wave based DFT. J Comput Chem, 2016, 37: 1030–1035
63 Maintz S, Deringer VL, Tchougréeff AL, *et al.* Analytic projection from plane-wave and PAW wavefunctions and application to chemical-bonding analysis in solids. J Comput Chem, 2013, 34: 2557–2567
64 Deringer VL, Tchougréeff AL, Dronskowski R. Crystal orbital Hamilton population (COHP) analysis as projected from plane-wave basis sets. J Phys Chem A, 2011, 115: 5461–5466
65 Dronskowski R, Bloechl PE. Crystal orbital Hamilton populations (COHP): Energy-resolved visualization of chemical bonding in solids based on density-functional calculations. J Phys Chem, 1993, 97: 8617–8624
66 Nelson R, Ertural C, George J, *et al.* LOBSTER: Local orbital projections, atomic charges, and chemical-bonding analysis from projector-augmented-wave-based density-functional theory. J Comput Chem, 2020, 41: 1931–1940
67 Spicer WE, Sommer AH. Intermetallic semiconductors containing alkali metals. J Phys Chem Solids, 1959, 8: 437–439
68 Huang HM, Liu TL. The transition from semiconducting to metallic characters in gold-alkali metal alloys. Phys Lett A, 1973, 46: 295–296
69 Watson RE, Weinert M. Charge transfer in gold–alkali-metal systems. Phys Rev B, 1994, 49: 7148–7154

Acknowledgements This work was supported by the National Natural Science Foundation of China (22073087, 12147105 and 22321001), the National Natural Science Foundation for Distinguished Young Scholars (22225301), Anhui Provincial Natural Science Foundation (2308085QB51), the Strategic Priority Research Program of the Chinese Academy of Sciences (XDB0450101), and the Fundamental Research Funds for the Central Universities (20720220007). We thank the support from the Super Computer Centre of University of Science and Technology of China and Supercomputing Center of Chinese Academy of Sciences.

Author contributions Wu X conceived the project. Zhang K carried out theoretical calculations. All authors wrote the paper and contributed to the general discussion.

Conflict of interest The authors declare that they have no conflict of interest.

Supplementary information Supporting data are available in the online version of the paper.

Kai Zhang is a postdoctor at Hefei National Research Center for Physical Sciences at the Microscale. He received his PhD degree from the University of Science and Technology of China in 2021. His research interest mainly focuses on the theoretical design of low-dimensional functional materials.

Xiaojun Wu is a full professor at the Department of Materials Sciences and Engineering, University of Science and Technology of China. He received his BSc degree and PhD degree from the Department of Physical Chemistry, University of Science and Technology of China. His research interest includes the development of materials design method, the design and computational simulation of spintronics materials, (photo)catalytic materials for energy, and other low-dimensional functional materials.

二维碱金属金化物双金属烯半导体

张凯[1,2], 吕海峰[2], 武晓君[1,2*], 杨金龙[1,2]

摘要 将不同金属元素通过合金化形成二维材料(金属烯)对基础研究和纳米电子器件的实际应用具有重要意义, 但目前鲜有金属烯材料是具有本征带隙的半导体. 受离子晶体成键特征的启发, 通过结构搜索、成键分析和高通量第一性原理计算, 本文从2500多个双金属烯中筛选出一系列具有晶格动力学稳定和碱金属-金离子键的二维碱金属金化物双金属烯半导体. 由于碱金属和金之间的大电负性差, 其中32个碱金属金化物双金属烯是带隙范围为0.97~5.20 eV的半导体材料, 而锂金双金属烯由于电负性差减小呈现出金属性. Bohn-Oppenheimer分子动力学模拟表明19个双金属烯在室温下结构稳定有利于实际应用. 这项研究为设计双金属烯半导体提供了指导, 并揭示了二维金属合金中成键行为和电子结构性质间的关联.

